Response inhibition is driven by top-down network mechanisms and enhanced with focused ultrasound

Justin M. Fine,[1*] Maria E. Fini, Archana S. Mysore,

William J. Tyler, Marco Santello

School of Biological and Health Systems Engineering,
Arizona State University, Tempe, AZ

[1]Current address: Psychological and Brain Sciences,
Indiana University, Bloomington, IN 47405

* Corresponding author: Justin M. Fine
Psychological and Brain Sciences
Indiana University
1101 E 10th Street
Bloomington, IN 47405
Email: justfine@iu.edu

Keywords: Cognitive control; Response inhibition; Transcranial focused ultrasound; Dynamic causal modeling; Prefrontal cortex.

Abstract

Response inhibition is necessary for humans to safeguard against undesirable action consequences. Inhibitory control consistently recruits the prefrontal right inferior frontal gyrus (rIFG) and pre-supplementary motor area. Yet, whether inhibitory control is a defining function of rIFG, distinct from attentional orienting, remains widely debated. The issue emerges from previous studies reporting inhibitory and attentional demands both elicit rIFG activation. Here, we address this issue based on the proposition that inhibitory and attentional control are predicated on different network mechanisms. We derived and causally tested network mechanisms using EEG, dynamic causal modeling (DCM) and focused ultrasound stimulation in humans performing a Stop-Signal task. rIFG stimulation increased inhibitory performance and speed. DCM of evoked responses linked behavioral inhibition to rIFG top-down gain modulation of pre-SMA inhibitory populations. These results reconcile competing accounts of prefrontal cognitive control function, by identifying rIFG-based inhibitory mechanisms as distinct from other top-down cognitive control processes.

Introduction

Response inhibition is necessary to stop unwanted actions (Logan & Cowan, 1984). Despite its ubiquity, it remains consistently debated about whether the brain implements behavioral inhibition as a distinct cognitive control process (Aron et al., 2014; Hampshire & Sharp, 2015; Mostofsky & Simmonds, 2008; Munakata et al., 2011). Prominent theories consider the right inferior frontal gyrus (rIFG) a central node in driving inhibition (Aron, 2011) alongside pre-supplementary motor area (pre-SMA) (Chikazoe et al., 2009). This is supported by imaging (Aron et al., 2006; Boehler et al., 2010) indicating rIFG scales with inhibtion and pre-SMA with action preparation (Rushworth et al., 2004) and lesion studies (Aron et al., 2003). However, alternative theories posit rIFG mediates context monitoring and attention (Hampshire et al., 2010; Munakata, Herd, Chatham, Depue, Banich, & O'Reilly, 2011). Supporting fMRI evidence indicates rIFG activates similarly across tasks involving inhibition and context monitoring, while pre-SMA activation still tracks inhibition (Erika-Florence et al., 2014; Sharp et al., 2010).

Here we propose that resolving this debate requires acknowledging that response inhibition and attentional orienting are throught to rely on different network mechanisms. Neural network models suggest response inhibition (Lo et al., 2009) could be directly implemented through top-down control over the recurrent gain of inhibitory interneurons. Indeed, neural circuits can exert inhibitory effects through feedback (i.e., top-down) connections to GABAergic interneurons (Bastos et al., 2012; Roux & Buzsáki, 2015) that mediate disinhibition of principal neurons (Lovett-Barron et al., 2012). In contrast, biased competition (Deco & Rolls, 2005; Desimone & Duncan, 1995)

and predictive coding models (Feldman & Friston, 2010) link attentional orienting to top-down gain modulation of neurons driving bottom-up responses. Neurophysiology (Thiele & Bellgrove, 2018) and biophysical connectivity models (Moran et al., 2013) further indicate top-down attention control over bottom-up responses coincides with gain modulation of cholinergic pyramidal cells in supragranular layers. It remains an open question whether either of these neural mechanisms can account for rIFG and pre-SMA interactions during response inhibition.

While neuroimaging studies have shown rIFG to pre-SMA connectivity scales with inhibitory success and speed (Duann et al., 2009; Rae et al., 2015), fMRI temporally filters the fast neural activity that underlies differences in response inhibition timing and success (Aron et al., 2014). Additionally, fMRI connectivity cannot differentiate top-down from bottom-up coupling or modulatory synaptic gain mechanisms. Although previous electrophysiological connectivity studies of inhibition have the proper temporal resolution, these approaches did not directly address synaptic gain mechanisms (Kibleur et al., 2016; Swann et al., 2011).

We address these gaps by combining neurostimulation of rIFG using high-resolution transcranial focused ultrasound (TFUS) with electroencephalography (EEG) to examine event-related potentials (ERPs) in humans performing a Stop-Signal task (Logan & Cowan, 1984). Several studies have shown the P300 ERP peak tracks the success of inhibitory outcomes (Bekker et al., 2005; Greenhouse & Wessel, 2013; Kok et al., 2004). However, because P300 peaks after stop responses, this amplitude modulation occurs too late to indicate inhibition per se. Others argue P300 amplitude reflects an outcome-monitoring (Huster, Enriquez-geppert, et al., 2013) or attentional

orienting process (Corbetta et al., 2008; Polich, 2007) that likely occur after inhibition. Recent evidence implicates P300 onset latency as a candidate marker of stopping processes because it tracks inhibition success and stopping speed (Wessel & Aron, 2015), and modulates before stop processes elapse. As we found here that TFUS improved stopping behavior through shortening the stop signal reaction time (SSRT), we predicted P300 onset latency would track the TFUS-induced changes in response inhibition success and SSRT.

We used ERP dynamic causal modeling (DCM; Moran, 2015) to determine whether rIFG deploys top-down inhibitory mechanisms that link modulation of P300 onset to inhibition and its speed. We arbitrated between frameworks by comparing models that included either top-down rIFG gain modulation over inhibitory interneurons predicted by direct inhibition models, superficial pyramidal modulation predicted by attentional frameworks, or a mixture. Accordingly, we hypothesized that if rIFG directly triggers inhibition and scales stopping speed, rIFG should modulate inhibitory interneuron gain in pre-SMA. Imperatively, this mechanism should scale with TFUS-induced effects on behavior. By modeling a network that included fronto-parietal and pre-SMA to rIFG connections, this allowed addressing whether pathways associated with attention were also modulated alongside direct inhibitory mechanisms.

Methods and Materials

Participants

Healthy adults (*n* = 63) were randomly assigned to one of three experimental groups. The main experimental group received transcranial focused ultrasound (TFUS)

stimulation to right inferior frontal gyrus (rIFG) (*n* = 25; 19 males, mean age = 24.1 yrs., SD = 3.2 yrs.). A second group received stimulation to the ipsilateral somatosensory cortex (*n* = 23; 15 males, mean age = 22.4 yrs., SD = 3.3 yrs.) and was used as the cortical site active control group (S1). A third group received sham stimulation near the right temple (*n* = 15; 8 males, mean age = 24.2 yrs., SD = 2.8 yrs.) and was used as control for possible auditory effects of TFUS (sham rIFG). All individuals were right-handed (self reported) and received financial compensation for participation in the study. Before enrollment, each subject was screened for neurological disorders and a history of epilepsy, stroke, or brain injury. A neurologist from Barrow Neurological Institute (Phoenix, AZ) screened all subjects' T1 MRI and cleared them before study participation.

Behavioral Task and Transcranial Focused Ultrasound design

Response inhibition was assessed using the Stop-Signal Task involving both 'Go' and 'Stop' trials (**Fig. 1**) programmed in Opensesame (Mathôt et al., 2012). Each trial started with a central fixation cross. In every trial, fixations were replaced by a green 'Go' circle (3° x 3° visual angle) after an exponentially-distributed time interval (range: 350-650 ms; mean: 500 ms; standard deviation: 50 ms). Subjects were instructed "to press the up key when detecting the Go circle" (**Fig. 1**). In 'Go' trials (rows 1-2, **Fig. 1**), the circle vanished either after the subject's response or 800 ms elapsed. In 'Stop' trials (rows 3-5, **Fig. 1**), the Stop signal was a red square which appeared around the green circle. If the subject successfully inhibited their response with respect to the Stop cue within 800 ms, the red square was extinguished, and the trial was considered a successful inhibition. The time required to inhibit a response following the Stop signal is

defined as stop signal reaction time (SSRT) (see below). Timing of the Stop cue relative to Go cue, i.e., the stop signal delay (SSD), was presented at one of four fixed, but subject-specific SSDs. The SSDs were chosen by having each subject perform a practice block of 50 Go trials to determine their baseline Go reaction time (RT). After this block, the 4 SSD levels were set to 25, 35, 75 and 95% of the mean Go RT. These SSDs were fixed throughout the experimental session and were presented in a random order across Stop trials. All trials were separated by a 2-s inter-trial interval (±300 ms random jitter).

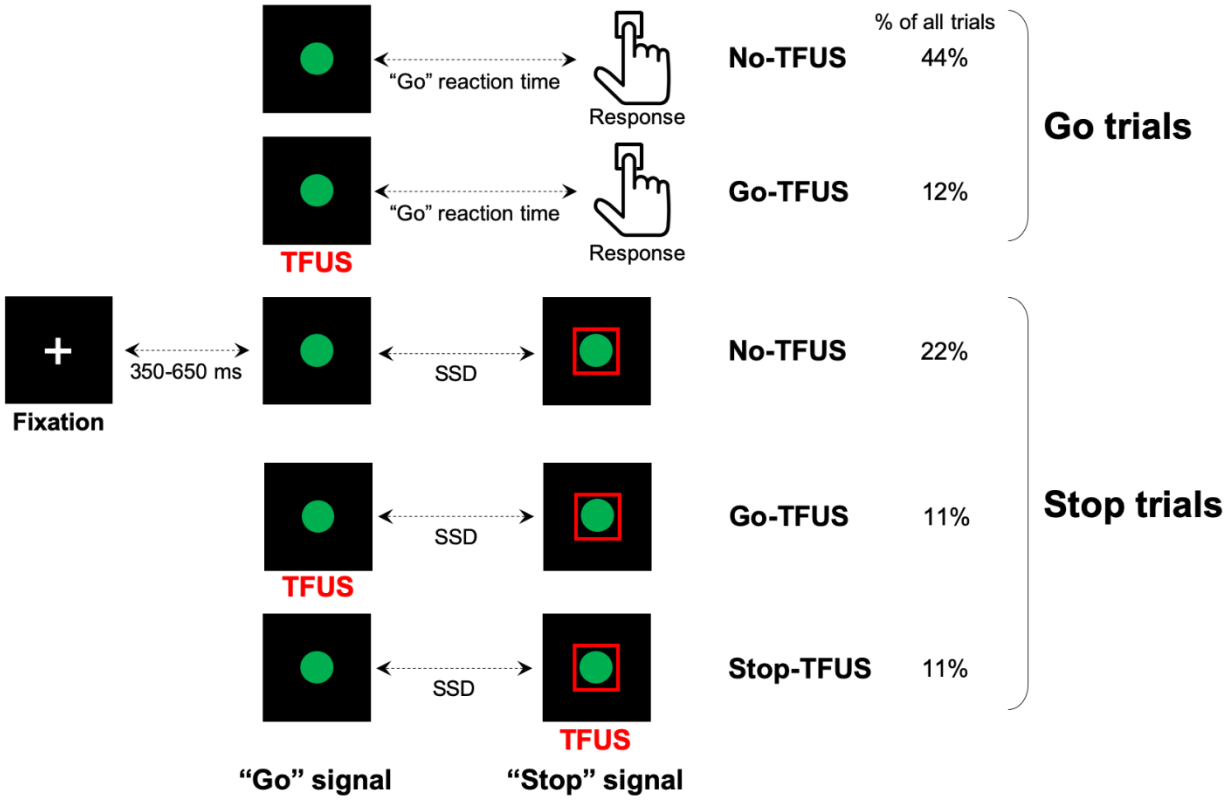

Figure 1 *Stop-Signal task and trial types: rIFG group.* Each trial type started with a fixation. After a randomly chosen delay (350-650 ms), subjects were asked to respond to a "Go" signal as fast as possible by pressing the up key. On a subset of trials (Stop trials; rows 3-5), a red square appeared at random latencies from the Go signal cueing subject to inhibit their response. Transcranial focused ultrasound (TFUS) was delivered to rIFG for 500 ms either at the onset of the Go (rows 2 and 4) or Stop signal (row 5). SSD: stop signal delay. The same design was used for two control groups (S1 and sham rIFG), although TFUS was not delivered to a cortical site in the sham rIFG group (see text for details).

We delivered Transcranial Focused Ultrasound (TFUS) either simultaneously with the Go signal in both Go and Stop trials, or the Stop signal (**Fig. 1**). This mixture of Go, Stop and TFUS delivery factors generated 5 trial types (**Fig. 1**). The first two consisted of Go trials with no TFUS or with TFUS time-locked to the Go signal (No-TFUS and Go-TFUS trials, respectively; rows 1-2, **Fig. 1**). The other three trial types consisted of Stop trials with no TFUS, and TFUS time-locked to either the Go or Stop signal (No-TFUS, Go-TFUS, and Stop-TFUS trials, respectively; rows 3-5, **Fig. 1**). TFUS delivery for Stop trials was evenly distributed across the 4 SSD levels. The overall probability of the occurrence of a Stop trial was 44% of all trials. This proportion of trials accommodates the need for a sufficiently large number of Stop trials to examine TFUS effects on Stop trials across all SSD levels, while enabling a more frequent occurrence of Go than Stop trials (56%; the percentage of each trial type is shown in **Fig. 1**).

Each experimental session consisted of 1200 trials distributed across 12 blocks of 100 trials each. Blocks were segmented into stimulation/no-stimulation and no-stimulation blocks, the former consisting of trials with and without TFUS, and the latter consisting of trials with no TFUS. Trial types (Go and Stop trials) were randomly distributed throughout the experiment. We chose a blocked design to mitigate possible carry-over effects of TFUS across trials. By using two control groups (S1 and sham rIFG), we could determine the extent to which behavioral and/or neural responses associated with TFUS were specific to the target site (rIFG).

EEG and structural imaging acquisition

EEG recording. EEG was recorded using a 64-channel ActiCap system (BrainVision, Morrisville, NC), with 10–20 layout. Data was recorded at a sampling rate of 5 kHz, with 0.1 μV resolution and bandpass filter of 0.1–100 Hz. Impedances were kept < 5 kΩ. Online recordings utilized a ground at AFz and left mastoid reference. At the beginning of each session, electrode layouts with respect to each individual's head shape were registered using the left and right preauricular, and nasion as fiducial landmarks. This allowed for later co-registration with each individuals T1 structural MRI scan and for source-localized analysis (see below).

Structural MRI (T1). For guiding TFUS neuronavigation and co-registering EEG electrode placement for source analysis and modeling, we obtained a structural T1 MRI scan for each participant. T1 volumes were collected using an 3D MPRAGE sequence (TR = 2300 ms, TE = 4.5 ms, 1 x 1 x 1.1 mm^3 voxels, field of view 240 x 256 mm^2, 180 sagittal slices) in a Philips Ingenia 3T scanner with a 32-channel head coil. Brainsuite was used to process T1s, which included cortical extraction sequence and a surface label-registration procedure with the BCI-DNI atlas. After labeling, we checked the locations and created a mask of either pars opercularis (rIFG group) or the centroid of ipsilateral S1 (S1 group). This volume labeling and mask creation procedure were used for guiding TFUS target identification.

TFUS targeting, setup and parameters

A BrainSight neuronavigation system (Rogue industries) along with subjects' T1 scans were used to guide placement of the focused ultrasound transducer beam profile for stimulation. This was done separately with respect to each individual's neuroanatomy and mask created from T1s. The first step involved creating a subject-

specific mask from cortical atlas registration and projecting into the Montreal Neurologic Institute (MNI) coordinate system. When planning the TFUS target, we considered both MNI coordinates and individual anatomy. For example, metanalysis studies have shown specific activation of the pars opercularis (around x=48, y=16, z=18) for contrasts of successful inhibition versus Go trials and successful versus failed inhibition trials (Chikazoe et al., 2009; Levy & Wagner, 2011). For the rIFG group, we first identified the pars opercularis MNI coordinates. During target planning, we confirmed the coordinates were inside the anatomical region of pars opercularis. We visually confirmed each subject's pars opercularis TFUS target was rostral to the inferior precentral sulcus and dorsal to the sylvian fissure, and ventral to the inferior frontal sulcus. For the S1 group, TFUS was targeted near MNI coordinates of x=-43, y=-29, z=54 and within the left post-central gyrus.

Before TFUS transducer setup, neuronavigation registered subjects' T1 scans in virtual space, with their head and the ultrasound transducer in real space. Alignment and cortical registration were performed using nasion, tip of the nose, philtrum, and left and right periauricular notch and tragus as fiducial landmarks. A 3D printed housing held the TFUS transducer, optical trackers, and silicon spacers (ss-6060 Silicon Solutions, Cuyahoga Falls, OH). Acoustic gel was applied to both transducer and scalp. We recorded stimulation target coordinates after placing the transducer in target alignment. In the sham rIFG group, we delivered sham TFUS (Legon et al., 2018) by placing the transducer perpendicular to the rIFG target. For the rIFG and S1 groups, we measured accuracy of stimulation target coordinates by tracking the deviation of the TFUS beam profile from the cortical target throughout the experiment. During the

experimental session, we sampled TFUS transducer spatial target deviation during each break. Accuracy was very high, with an average deviation of ±1.5 mm displacement across all subjects and sessions.

Our TFUS setup and parameters were nearly identical to those used in Legon et al. (2014). Briefly, we used a single-element TFUS transducer with a center frequency of 0.5 MHz, focal depth of 30 mm, a lateral spatial resolution of 4.5 mm^2, and axial spatial resolution of 18 mm^2 (Blatek, Inc., State College, PA). TFUS waveforms were generated using a two-channel, 2 MHz function generator (BK Precision). The system operated by channel 1 produced a pulse repetition frequency (PRF) of 1.0 kHz. Channel 1 also triggered channel 2, which produced short bursts at the 0.5 MHz acoustic frequency. This produced an ultrasound waveform with a carrier frequency of 0.5 MHz, PRF of 1.0 kHz, and duty cycle of 24%. Each stimulation duration was 0.5 s. Transducer power was driven by output from a 40-W linear RF amplifier (E&I 240L; Electronics and Innovation). It has been previously verified that the resulting waveform does not cause heating of skin or skull bone (Legon et al., 2014).

Computational simulation and validation of TFUS propagation

We quantified peak pressure amplitude, peak intensity and accuracy of the TFUS beam distribution delivered to rIFG using the pseudospectral simulation method in K-wave (Treeby & Cox, 2010). Reference peak pressure planes for the simulations were derived from previous data (Legon et al., 2014). Simulation parameters were first validated by simulating the transducer in water to compare the simulation results with those from previous water tank tests (Legon et al., 2014). The maximum pressure plane at the 30-mm focus was used as a source input pressure for the transducer during the

simulation. The transducer was modeled to have a 30-mm radius of curvature. For water simulations, we used a homogenously medium of water density (1000 kg/m^3) and speed of sound (1482 m/s). We created a computational grid over a 256 x 256 x 256 with 1-mm spacing. The points per wavelength were 6, Courant–Friedrichs–Lewy = 0.1, and simulation time was set to 6 pulses (duration = 250 μs) to ensure simulation stability.

For simulating transcranial ultrasound stimulation, we extracted 3-dimensional maps of the skull from a CT (1-mm resolution) and brain from T1 MRI scans (1-mm resolution) from three preoperative patients at Barrow Neurological institute. The MRI and CT were both co-registered and normalized to the MNI space in SPM12. To mimic our approach of TFUS targeting used in the experiments, we surface registered the gray matter volume to the BCI-DNI atlas and identified the centroid of pars opercularis. The average stimulation location for these three subjects was x = 48, y = 18, and z = 6. This allowed us to map from world coordinates of the scan to MNI coordinates of the target. **Figure 2A** shows T1 and scalp from one subject, together with renderings of the transducer housing, the pars opercularis mask, and the TFUS target applied to all MRIs from the rIFG group. **Figure 2B** shows side views of non-normalized T1s, pars opecularis masks, and the TFUS targets (red dots) for four subjects (**Figure 2B**). Conversion from Hounsfield units in the CT to sound speed and density were done using the relations described in Aubry et al (2003). All skull materials were set using these parameters, while other tissues were treated as homogeneous with parameters set to that of water. Attenuation was modeled as a power law with a β = 0.5 while absorption was modeled with *b* = 1.08 (Treeby and Cox, 2010).

To assess transcranial stimulation accuracy, the simulated transcranial transmission was compared against simulations of TFUS transmission through water. Differences between these simulations shows the estimated effect of any power absorption and change in acoustic profile after skull transmission. Numerical simulation parameters (see above) were derived to ensure the water simulation here matched the water tank results from a previous study using the same transducer and TFUS experimental parameters (Legon et al., 2014). Simulation of ultrasound through water predicted a max pressure of 1.05 Mpa, spatial peak pulse average intensity (Isppa) of 22.4 W/cm^2 at the focus, and lateral full-width at half maximum of the maximum pressure of 4.39 mm (**Fig. 2C**).

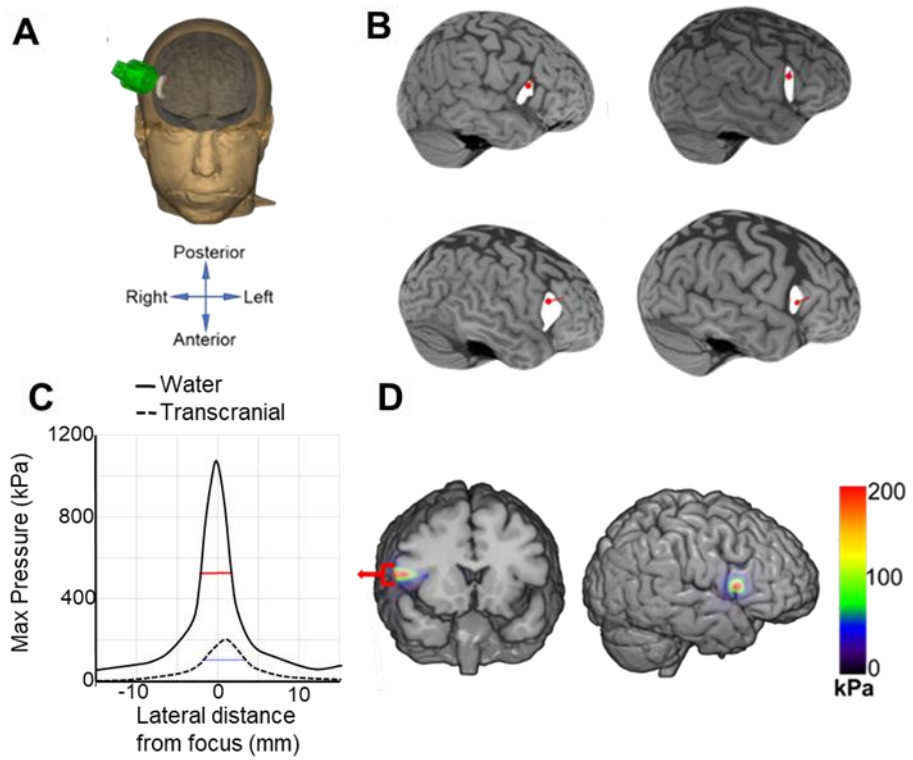

Figure 2 *TFUS targeting and simulation.* **A**. Average neuronavigation location of TFUS (red dot) applied to all MRIs used in the rIFG group. **B**. Structural brain scans and renderings of the targeted TFUS point (red dot) in pars opercularis (4 subjects). **C**. Lateral maximum pressure profile obtained at 30-mm depth focus in both water and TFUS simulations on a CT scan from one patient (solid and dotted lines,

respectively). Horizontal red and blue lines denote full-width half maximum of the spatial profile of lateral pressure. **D**. Simulated transcranial pressure profile onto T1 MRI plot shown as a color overlay.

Comparison of simulations and previous water tank data (Legon et al., 2014) using the same transducer and experimental TFUS parameters indicated a 97% match of pressure/intensity at the focus taken over a 5 mm^3 voxel section in all 3 planes at the focus. Next, modeling of transcranial transmission predicted an average maximum intensity of 2.8 W/cm^2, which is the intensity range of non-thermal neuromodulation and that exhibits nearly instantaneous measurable effects on EEG (Legon et al., 2014). Comparing the water and transcranial simulation, accuracy was assessed by comparing shifts in peak pressure. Skull transmission compared to water was shifted 1.25 mm laterally and had a lateral beam profile full-width half maximum of 5.1 mm (**Figure 2C**). These transcranial simulations indicate high spatial precision, with >95% of pressure or energy (kPa) being constrained to pars opercularis in the rIFG group (**Fig. 2D**).

Statistical analysis

Behavioral variables*.* Our behavioral analyses focused on the following variables: Go trial reaction time (Go RT), percentage of successfully inhibited responses on Stop trials (successful stopping) per SSD, failed inhibition reaction time, and SSRT. The SSRT was estimated using a hierarchical Bayesian parametric approach (Matzke et al., 2013a) that estimates distribution of SSRTs while assuming an ex-gaussian parametric form. We chose this approach as Matzke et al. (2013a) showed that it performs well even when there are only a few trials available per SSD level. This SSRT estimation procedure was run separately per group (rIFG, S1, and Sham rIFG) and trial types (No-TFUS Stop trials, Go-TFUS Stop trials, and Stop-TFUS Stop trials; **Fig. 1**). As

we report in the Results section, we used Go RTs combined from Go trials with and without TFUS because stimulation did not alter the Go RT.

The probability of response inhibition changes over levels of SSD, P(respond|signal), and across TFUS conditions were assessed within and across groups by fitting a 2-parameter logistic mixed effects model with random intercepts and slopes to obtain subject- and condition-specific model parameters. P(respond|signal), denoted as p, were converted to a negative logit ($\log((1-p)/p)$) before fitting. As our main goal was to estimate the logistic curve slope (**β**), we ran the mixed-effects model (using LME4 in R) with the full interaction of SSD and stimulation condition in the three Stop trial types (no-TFUS, Go-TFUS, Stop-TFUS). Logistic slopes per subject were estimated by combining fixed and random coefficients. **β** parameters were analyzed using a mixed-design ANOVA on **β** with factors of Group (3 levels) and TFUS (3 levels: No, Go, Stop).

EEG pre-processing

Continuous EEG data were first down-sampled to 250 Hz, then high-pass filtered (0.1 Hz) and re-referenced to the scalp average. Any channels that displayed artifacts for more than 25% of the total session were removed before further processing, but were later interpolated after artifact rejection. We removed channels that were designated unsuitable for analysis by visual inspection and absolute temporal standard deviation (> 5) across channels. It is important to note that, in each of the stimulation groups, the cortical sites of rIFG and S1 were close to the F8 and CP4 electrodes. Therefore, these electrodes could not be used for EEG recording in their groups and were interpolated after artifact removal. Remaining data were epoched from Stop trials

locked to stop signal onset (-200 to 600 ms peristimulus). Individual epochs were rejected from analysis if they contained large scalp EMG or rare events (< 8% of all trials). Out of the 63 participants, 3 subjects were excluded from analyses due to EEG recording issues (impedance >25 kΩ across channels). The remaining data were bandpass filtered from 0.5-40 Hz. EOG artifacts were removed using Independent Components Analysis using eeglab (ICA; Delorme & Makeig, 2004). On average, 3.35 components were removed per participant. Remaining ICA components were back-projected to electrodes and then averaged to create event-related potentials (ERPs) per condition, e.g., different SSD levels for No-tFUS Stop trials). The ERPs baseline were normalized by subtracting the activity from -100 ms to the Stop signal onset. Because we later applied a Hanning taper to the edges of the ERPs before dynamic causal modeling, we applied the same procedure to ERPs after cleaning using a Hanning taper.

Isolating inhibitory response ERPs

Our analysis focused on sensor, source, and source network models of ERPs because several types of ERPs have been linked to the success and speed of stopping. Due to the macroscopic nature of EEG signals, there is likely a temporal overlap of neural processes related to stopping and going during Stop trials. We aimed to separate Go-related activity from Stop-related activity separately for both successfully (SS) and unsuccessfully (US) inhibited Stop trials. This was done by subtracting the Go trial ERPs from the Stop trial ERPs, and using the approach employed by Mattia et al (2012). On a per-subject basis, we found Go-trial ERPs (No-TFUS and TFUS) whose RTs matched those of SS trials based on each subject's SSRT. These Go trials had to

have RTs either equal to or greater than the SSRT. For US stopping trials, we found latency-matched Go trials with RTs by first calculating each subject's mean signal-respond RT for each of the two highest SSDs. We then calculated the difference in SSD (ms) and searched for Go RT trials for each SSD that fell within the mean signal-respond RT ± half the difference of the SSD (ms). This was done to prevent overlap of activity from both faster and slower Go RTs and signal-respond RTs. These steps were performed separately for the highest and second highest SSD. This procedure was done separately for SS and US trials for both No-TFUS and TFUS conditions. After correcting the SS and US stop trial, the corrected ERPs were averaged across the two highest SSDs per subject (corresponding to 85% and 105% of mean Go RT of each subject). These ERPs were used for the remaining analysis.

ERP analysis

Sensor-space analysis. We examined ERPs at the sensors level using permutation-based dependent samples t-tests that account for spatiotemporal clustering. We performed tests utilizing multiple comparisons with cluster-based p-value corrected at $p < 0.01$, and performed 5000 permutations for each contrast. We used two different contrasts to analyze differences for stopping success overall and TFUS effects on ERPs. The contrasts included comparison of (1) SS –US trials collapsed over No-TFUS and Stop-TFUS conditions, (2) a TFUS effect comparison of SS (No-TFUS) – SS (Stop-TFUS) contrast, and (3) the interaction contrast of SS – US trials with No-TFUS and Stop-TFUS. The first contrast is typically used to determine which areas exhibit ERPs (or brain areas) that differentiate successful inhibition. The second contrast was used to determine which scalp ERPs differentiated successful stopping in the No-TFUS

and Stop-TFUS conditions. The third contrast (interaction) was used to determine how the SS-US contrast differed between No-TFUS and Stop-TFUS conditions. The second and third contrasts were the primary focus of our analyses and expected to provide the most direct indication of inhibitory-specific ERP effects. Our reasoning was as follows: if the first SS-US contrast reveals ERP activity and latencies that differentiate successful and failed inhibition, and TFUS alters the potency of inhibitory processes and ERPs that differentiate the level of successful inhibition (second contrast) , the interaction contrast should isolate changes in neural response strength to Stop signals and behavioral inhibition outcomes that are jointly modulated by TFUS.

Because recent work has indicated the frontocentral (ERP) P300 onset latency, rather than peak amplitude, is related to the stopping speed (SSRT) across-subjects (Wessel and Aron, 2015), we regressed the between-subject changes in SSRT as a function of the P300 latency change between No-TFUS and Stop-TFUS. To achieve this, we computed the shift in P300 onset crossings between No-TFUS and Stop-TFUS conditions in two steps. First, we took the across-subject mean frontocentral ERP waveform in a time-window of ±50 ms around the zero crossing. To calculate each subject's zero-crossing time, we calculated the dynamic time warping distance from the template mean ERP to the subject's ERP. Second, this distance was added to the median zero-crossing time to obtain an individual subject crossing for both the No-TFUS- and Stop-TFUS conditions. These changes in P300 onsets were then regressed against individual subject differences in SSRT between conditions.

Source-localization and source statistics. To localize source generators of ERPs differentiating inhibitory outcomes and provide initial locations for our network

connectivity, we estimated the ERP activity in source space. This step employed a multiple sparse-priors approach as implemented in SPM12. The approach estimates the cortical source activity of sensor ERPs from the SS and US trials across TFUS conditions. We chose this Bayesian estimation method because it has been shown to have good accuracy during simulation recovery studies (Belardinelli et al., 2012). Furthermore, this method focuses on finding the simple, sparse solutions given the ill-posed nature of source localization. We used cortical meshes to calculate the EEG forward solution using a boundary element head model based on each subject's T1. Source inversion was performed over a window starting from the Stop signal up to 450 ms to capture activity occurring over the whole stopping period. This window of source data was converted to a 3D image, spatially smoothed (8 mm full-width half maximum) and interpolated into MNI voxel space for each subject and condition. This was converted into a statistical parametric map (SPM) and analyzed used a flexible factorial design to implement a repeated-measures ANOVA to examine the main effect of inhibition success (SS or US trial). The resulting SPM was analyzed with a threshold set at $p < 0.005$ (peak-level, uncorrected) and cluster-wise family-wise error rate $p < 0.05$.

Dynamic Causal Modeling

Dynamic causal modeling (DCM) was used to analyze different neural models of effective connectivity. We applied this approach to determine the network changes underlying successful inhibition and how they unfolded during successful stopping in both No-TFUS and Stop-TFUS conditions. Furthermore, we used the DCM to examine how different sources and their connectivity under response inhibition and TFUS

conditions lead to the generation of ERPs linked to successful stopping with a focus on the P300.

DCM is a source analysis that estimates how each neural source – modeled using biophysically-based neural mass models – and their connectivity relates to measured ERP sensor data. DCM has now been applied in many studies to examine effective source connectivity using EEG and MEG data (for overview see Moran, 2015). The approach uses Bayesian source model evidence to map the estimated source data to the sensor data by using the lead field generated based on each subject's T1 MRI. Because DCM attempts to explain the measured data, we can compare and optimize different source activity networks and connectivity structures to infer the most plausible explanation for the data as is routine in modeling procedures. Additionally, because DCM for ERPs derives from physiological models driving source activation and connectivity, while using a forward model mapping source to sensor space, it is valuable for differentiating how connectivity changes drive ERPs in experimental conditions.

Sources were based on previous neuroimaging studies of inhibition tasks, and the MNI locations used in the DCM were based on those found in our source analysis (see Results). We used source analysis areas that have been previous linked to inhibitory and attentional control (Corbetta and Shulman, 2001; Swaan et al., 2009; Wessel and Aron, 2017). This analysis revealed evoked power differences during inhibition in areas conforming to the right lateralized network typically found during inhibition (Boehler et al., 2010; Levy & Wagner, 2011b; Sharp et al., 2010). Locations included rIOG, rIFG, rTemporal, rParietal, and pre-SMA, with the source analysis results used as source locations in the DCM. The MNI coordinates employed in the DCM for

each source included rIFG ([48,28,4]), pre-SMA ([0, 24, 54]), rParietal ([40,-54,50]), rTemporal ([52,-18,-12]), and right inferior occipital gyrus (rIOG) ([46, -76,10]). These locations are in strong agreement with those found in meta-analyses of inhibitory control tasks (Rae et al., 2014).

Sources were modeled with the canonical microcircuit neural mass model that has been shown to embody hierarchical Bayesian predictive coding theories of brain function (Bastos et al., 2012). This model has been used extensively to model EEG/MEG connectivity during studies of attention and stimulus prediction (Auksztulewicz & Friston, 2015; Brown et al., 2013). The model implements source data generation as four distinct neuronal populations that include the superficial and deep pyramidal cells, spiny stellate cells, and inhibitory interneurons. Each of these layers also has recurrent inhibitory gain connections that model layer-specific inhibitory neurons. Connectivity between each population is derived from laminar-specific connectivity patterns in the cortex (Douglas & Martin, 2004; Felleman and Van Essen, 1991; Shipp, 2007). Because connections between sources are implemented as either forward (i.e., bottom-up) or backward/feedback (i.e., top-down) connections, this allows us to distinguish how specific types of connectivity are altered during both successful inhibition and as a result of TFUS.

Central to using this DCM approach was arbitrating between neural mechanisms required for a direct inhibitory control model versus an attentional control model (see Introduction). Specifically, we were concerned with the top-down interaction between rIFG to pre-SMA and temporal cortex. Both frameworks and physiology suggest a rIFG driven top-down, activity-dependent modulation of the recurrent gain in pre-SMA. Direct

inhibition models predict rIFG descending activity should alter inhibitory interneuron gain in pre-SMA. Conversely, attentional models predict rIFG descending activity should directly alter recurrent gain of superficial pyramidal populations that drive bottom-up excitation. However, previous work proposing rIFG as driving attentional reorientation does not specify what the neural target of rIFG modulation would be. For example, attentional modulation could follow from rIFG modulation of temporal cortex or pre-SMA, and having a chain effect on parietal areas also responsible for attentional control. However, such a mechanism likely operates alongside a direct inhibition from rIFG to pre-SMA. To address all of these possibilities, we considered several permutations of models in which the gain was modulated either independently of top-down activity (e.g., pre-SMA isolated gain changes), or was modulated by top-down activity from other sources (e.g., from rIFG to pre-SMA). We also considered whether these gain changes occurred in superficial pyramidal or inhibitory interneuron populations estimated within a source, and considered several different mixture variants. For example, some models had rIFG modulate inhibitory interneuron gain in pre-SMA and pre-SMA exerting gain modulation over parietal superficial pyramidal units.

Model building first involved estimating the connectivity structure best explaining the ERP data (DCM ‘A’ matrix), determined using a series of Bayesian model selections with family-wise random effects (Penny et al., 2010) by fitting each DCM to each subject’s No-TFUS successful inhibition trials in a time window spanning 0-450 ms (0 = Stop signal onset). We chose these trials as a baseline condition to determine the optimal model without effects due to TFUS. Model spaces were partitioned into several families based on a (1) pre-frontal hierarchy structure, (2) structure of the lower

hierarchy, (3) connections from lower areas (rTemporal and rParietal) to higher areas (rIFG and pre-SMA), and (4) whether exogenous gaussian bump inputs were in either rIOG and rIFG, or just rIOG.

We further optimized the model again to estimate the condition effect modulation on recurrent gain and extrinsic connections (‘B’ matrix) that differentiated successful and unsuccessful inhibition. The optimized DCM structure were fit to individual subject’s ERPs for both the No-tFUS successful and failed inhibition trials together. The effects of intrinsic gain were examined over two families. The first family was modulation in superficial pyramidal versus inhibitory interneurons. The second family assessed whether the post-synaptic gain effects were activity-independent or activity-dependent. Activity-independent gain effects presume gain changes are independent of direct activity from other areas, and it is assumed to align with local neuromodulatory concentration effects (Moran et al., 2013), e.g., acetycholine or dopamine concentration. In contrast, activity-dependent effects result from an area’s gain alterations resulting from top-down descending activity levels, hence making these gains voltage dependent. All of these effects were tested combinatorically over all areas, such that some sources could have superficial or inhibitory populations modulated either in an activity-independent or -dependent fashion. The failed inhibition trials were treated as a baseline when modeling these effects. Rather than optimizing the extrinsic connections before statistical analysis, we allowed them all to modulate between conditions (inhibition success) as their effective changes were tested using a hierarchical model across subjects (see below). After determining the DCM gain effects, the finalized DCM

were fit to individual subjects' ERPs across successful and unsuccessful inhibition trials, as well as No-TFUS and Stop-TFUS conditions.

Analysis of DCM results

To analyze the resultant condition-specific connectivity changes, we employed the Parametric Empirical Bayes (PEB) framework (Friston et al., 2016). PEB is a general linear hierarchical modeling approach, which we used to perform hypothesis testing regarding how connectivity parameters both changed on average between No-TFUS and Stop-TFUS conditions, and corresponded to scaling of stopping efficiency (SSRT). Rather than considering all possible connections, we constrained the analysis to those top-down effects involving rIFG, and pre-SMA to parietal connections. We chose this subset of connections because they correspond to the core interactions underlying our hypotheses. Once the group-level GLM parameters were estimated with respect to modulation of extrinsic and intrinsic connectivity, hypothesis testing proceeded using Bayesian model reduction of the GLM. This involves turning off/on different parameters and comparing free energy of reduced models, similar to performing model likelihood ratio tests commonly used in mixed-modeling. At a design level, we tested for mean connectivity effects differentiating successful and failed inhibition and their interaction with TFUS conditions. The interaction term was also examined with respect to SSRT and mean effects. This addresses the expectation that a connection directly related to triggering inhibition and scaling its potency should be predicted by behavior in No-TFUS trials and behavioral changes in TFUS trials. After model reduction, the reported PEB model parameters were computed through Bayesian model averaging and cutoff to effects having a >95% posterior probability.

Results

Human participants performed a Stop-Signal task and received online transcranial focused ultrasound (TFUS) on a subset of Go and Stop trials (**Fig. 1**). Subjects were divided into groups according to TFUS stimulation type: (1) an experimental group that received active stimulation to right pars opercularis (rIFG), (2) a control group that received active stimulation to ipsilateral primary somatosensory cortex to account for non-site specific TFUS effects (S1), and (3) a second control group that received sham stimulation to account for possible TFUS-induced auditory artifacts (sham rIFG). Stimulation was applied online at the onset of “Go” or “Stop” signals, separately for both Go and Stop trials (**Fig. 1**). We hypothesized that if rIFG drives motor inhibition, TFUS behavioral effects would be limited to alteration of stopping during TFUS applied simultaneously with the Stop signal.

TFUS to rIFG improves stopping behavior

We first addressed how probability of failing to inhibit responses, P(respond|signal), changed across TFUS conditions (No-, Go-, and Stop-; rows 3-5, **Fig. 1**) and groups, by fitting a 2-parameter logistic mixed-model to obtain response inhibition curve slopes (**β)** across subjects and TFUS conditions. Analysis of **β** revealed only the rIFG group exhibited a TFUS-altered P(respond|signal), consisting of an enhanced ability to inhibit reponses relative to the control groups. ANOVA results indicated a significant Group x TFUS interaction ($F(2,50) = 3.8$, $p = 0.034$, $\eta_p^2 = 0.17$), and an overall effect of TFUS condition ($F(2,50) = 11.74$, $p = 0.002$, $\eta_p^2 = 0.29$). Follow-up one-way within-group ANOVAs across TFUS conditions showed only the rIFG group exhibited differences across the different TFUS conditions. T-tests in this group showed

β for Stop-TFUS was lower than No-TFUS and Go-TFUS conditions (both $p < 0.01$: mean **β**'s indicating change in probability for approximately 25% change in normalized SSD: No-TFUS = 0.35 (0.12), Go-TFUS = 0.35 (0.11), Stop-TFUS = 0.27 (0.08)) (**Fig. 3A**). Therefore, TFUS effects were limited to the rIFG group and Stop-TFUS trials.

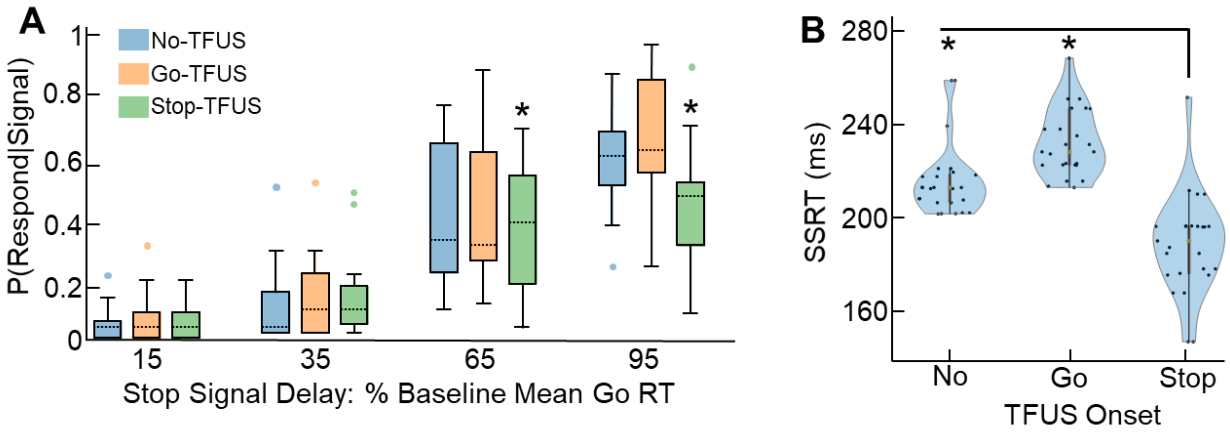

Figure 3 *Behavioral effects of TFUS: rIFG group.* **A.** Probability of responding across Stop signal delays for TFUS delivered on Stop trials. **B.** Violin plots of across-subject distribution of Stop signal reaction times (SSRT) across the TFUS conditions used for Stop Trials.

The effects of rIFG TFUS improvements on successful inhibition performance apper greater at longer SSDs (65% and 95% SSD; **Fig. 3A**). A repeated-measures ANOVA on P(respond|signal) for rIFG group across SSD levels and TFUS onsets supported this with a significant interaction ($F(6,102) = 8.21$, $p < 0.0001$, $\eta_p^2 = 0.33$). T-tests between Stop-TFUS and the average of No- and Go-TFUS across all SSDs indicated the interaction resulted from a reduction in P(respond|signal) for Stop-TFUS in the two longest SSDs (all $p < 0.01$; Bonferroni $\alpha = 0.0125$). These results indicate Stop-TFUS induced improvements of inhibition were more pronounced at longer SSDs (**Fig. 3A**).

Based on the prediction that rIFG drives an inhibitory process and our finding that TFUS improved response inhibition only in the rIFG group, we hypothesized rIFG TFUS changes to P(respond|signal) should result from a shortening of the stopping speed, i.e., SSRT. Notably, TFUS did not affect other behavioral variables, e.g., Go RTs. SSRT analysis in a mixed-design ANOVA indicated a significant Group x TFUS interaction ($F(4,100) = 10.2$, $p < 0.001$, $\eta_p^2 = 0.21$). Follow-up one-way ANOVAs within groups indicated only rIFG group SSRTs (**Fig. 3B**) significantly differed across TFUS conditions ($p < 0.05$), with t-tests confirming that SSRTs were indeed shortest and only altered for Stop-TFUS trials (**Fig. 3B**). This indicates TFUS delivered to rIFG concident with the Stop signal altered inhibition by shortening the SSRT.

We used separate analyses to determine whether P(respond|signal) changes from TFUS were also affected by non-inhibitory behaviors. We first addressed whether TFUS within the rIFG, S1, and rIFG sham groups exerted any effects on simply responding to the Go signal by extracting mean RT from ex-gaussian distributions fit using maximum likelihood (Lacoutoure and Cousineau, 2008). Means for each subject were analyzed using a 3 $\times$ 2 mixed-design ANOVA with factors of Groups (3) and TFUS condition (2: No-TFUS, Go-TFUS trials). This analysis allowed us to assess if “going”, independent of “stopping”, was altered by potential TFUS auditory artifacts (sham rIFG group), stimulation to unrelated areas (S1 group), or whether TFUS to rIFG also influenced Go RT processes independent of a stopping context (rIFG group). We found no significant effect of TFUS condition, group, or their interaction (all $p > 0.05$). These results suggest that neither TFUS (rIFG and S1 groups) nor auditory factors alone (sham rIFG group) altered Go RTs independent of a Stop signal.

Improvements in inhibition from TFUS could also have emerged from longer SSRTs or reduced SSRT variability. Two mixed-design ANOVAs were used to examine the subject-level SRRT means and variability with Group (3 levels) and TFUS (3 levels: No-TFUS, Go-TFUS, Stop-TFUS). We found no significant interactions or effects of TFUS on SRRT or its variability. Together, these behavioral results indicate that only TFUS to rIFG improved response inhibition by shortening a process related to the stopping speed.

Neural responses underlying inhibition

We will now focus only on the rIFG group because this was the only group exhibiting behavioral TFUS effects. Furthermore, we only analyzed No-TFUS and Stop-TFUS conditions because Go activity was subtracted from neural data from Stop trials (see Methods). Sensor-level ERPs were examined in this group across three contrasts using cluster-based permutation t-tests: (1) successful – unsuccessful stopping contrast over each TFUS conditions, (2) successful (No-TFUS) – successful stopping (Stop-TFUS) contrast, and (3) interaction comparing successful – unsuccessful stopping between the No-TFUS and Stop-TFUS conditions. The average activity of ERP time-windows and voltage deflections of an N200 and P300 that are typically found during inhibition (Kenemans, 2015) are shown in **Figure 4A**.

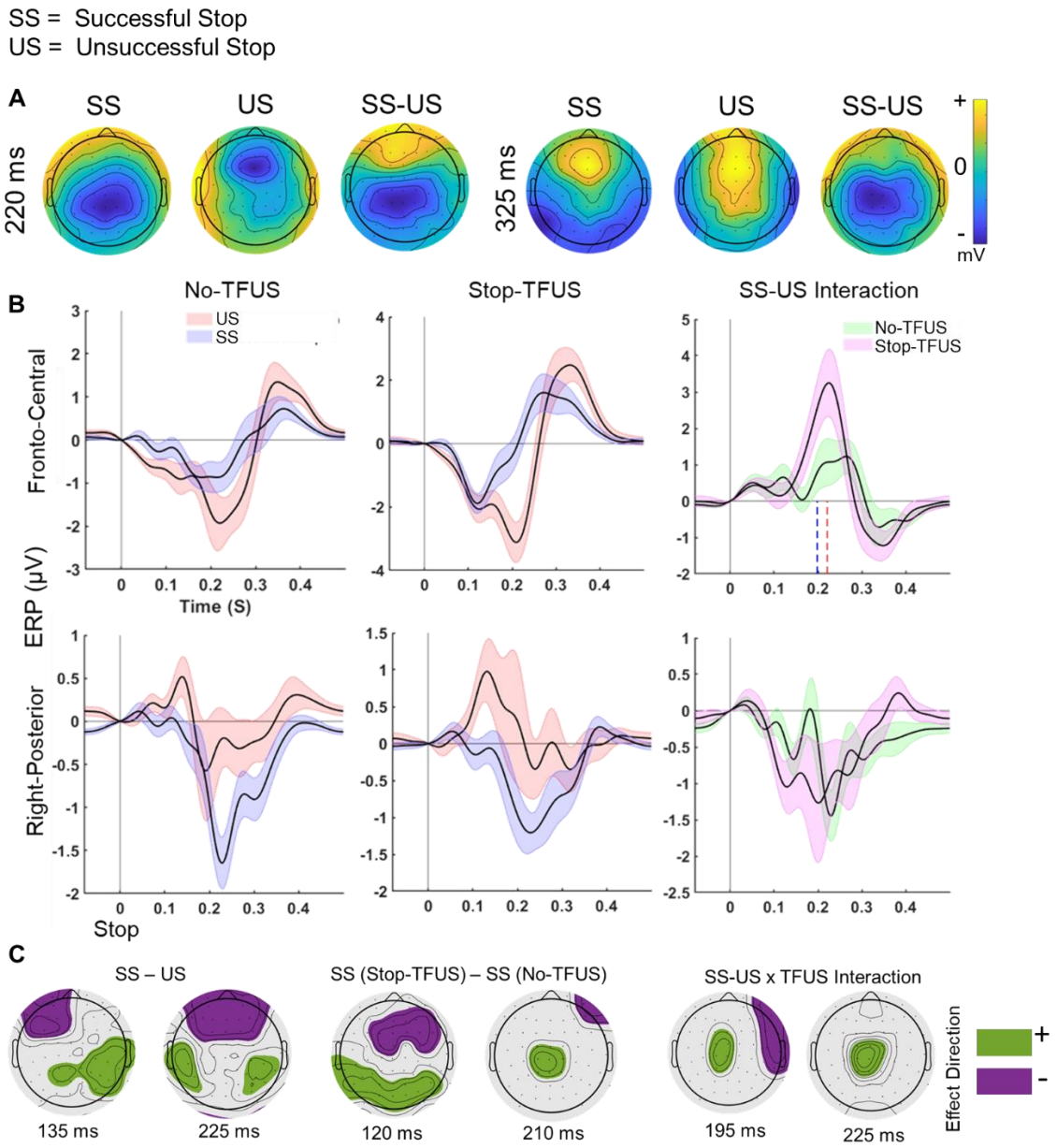

Figure 4 *Effects of TFUS on ERPs during successful and unsuccessful response inhibition.* **A.** Average scalp maps of successful (SS), unsuccessful (US), and SS-US difference maps showing ERP amplitude at time points aligned with canonical ERP effects associated with response inhibition. **B.** Average ERP plots for two a-priori chosen regions of electrodes to capture the typical N200/P300 ERP in Fronto-Central electrodes (Cz and Fcz; top row), and N100 sensory responses in Right-Posterior (CP4 and P4; bottom row). Plots show mean ERPs for SS and US trials across TFUS conditions (left and middle columns) and their interaction (right column). In the right column, the dashed vertical lines denote the median SSRT across subjects for the No-TFUS (red line) and Stop-TFUS (blue line) conditions under the interaction in Fronto-Central electrodes (top row). **C.** Permutation sensor t-tests showing the maximal effects for three comparisons: SS-US, SS trials across TFUS conditions, and interaction effect of SS-US and TFUS.

We observed an early (100-150 ms) right-posterior P100 response peaking around 135 ms that differentiated successful from unsuccessful stopping (SS and US, respectively; **Figure 4B**, left plot of **Figure 4C**). Peak location and timing are indicative of a visual P100, visible in average time-course and t-stat map (**Figure 4B-C**), with larger peak amplitudes in US trials. Contrasts of SS trials across TFUS conditions revealed the P100 was smaller on Stop-TFUS SS trials (**Figure 4C**, middle). A difference in SS trials was found for N100 responses in both frontal and right-frontal electrodes (**Figure 4C**, middle). N100s were generally larger for the Stop-TFUS trials. Neither of these ERPs exhibited an interaction of SS-US and TFUS trials. These results indicate smaller amplitudes of early sensory responses predicted successful stopping, but the lack of interaction indicates they were not directly related to inhibition.

The ERPs typically associated with indexing inhibition is the N200/P300 complex. Notably, this complex often appears in a fronto-central cluster, with the N200 peak being most prominent during failed stopping. The fronto-central ERP plot shows the N200 peaks around 200 ms but does so most clearly in US trials (**Figure 4B**, top row). Comparing SS and US trials supported this effect of larger N200 during US trials (**Figure 4C**, left). Contrasting SS trials across TFUS conditions indicated this ERP was larger for the No-TFUS condition. The interaction effect (**Figure 4C**, right) indicated the maximal difference corresponded to N200 timing, exhibiting a larger difference in the SS-US contrast during Stop-TFUS trials. N200 amplitude decreased with increasing inhibitory performance, with the smallest peak in Stop-TFUS SS trials (**Figure 4B**, top row). The fronto-central P300 also differentiated SS and US trials, with a lower

amplitude for US trials. The lack of interactions for the P300 indicated it was distinct from driving the strength of inhibition.

Our main ERP hypothesis was that P300 onset timing, rather than its peak, reflects an inhibitory process. This hypothesis stems from two considerations. The first is the N200 and P300 likely reflect a mixture of underlying components with the N200 amplitude being reflected in the P300 onset. In this case, a shift in P300 onset would drive our observed interaction contrast of the fronto-central N200 by altering the time of the N200 peak amplitude. Examination of the time course of fronto-central ERPs (**Fig. 4B**, top row) indeed indicated that reduction in N200 amplitude is likely driven by the P300 onset occurring earlier. The second considerations is that an inhibitory marker should track inhibition timing (SSRT), which has been previously reported for P300 onsets (Wessel & Aron, 2015). Therefore, we predicted that the P300 onset latency should correlate with the SSRT difference across TFUS conditions. Visually contrasting SS-US difference waveforms across TFUS conditions (**Fig. 4B**, upper right) revealed P300 onsets shifted earlier during Stop-TFUS. We found TFUS-induced changes in P300 onset significantly correlated with SSRT (0.61, $p < 0.05$), thus providing direct support of P300 latencies tracking inhibition speed.

Dynamic Causal Modeling of ERPs in the inhibition network

The combined effects of TFUS on behavioral and evoked responses indicated inhibition performance improved together with a shortening in SSRT, which was matched by a shorter P300 onset latency. Given TFUS to rIFG altered inhibition, a core question is to what extent rIFG network interactions drive these evoked responses and associated behavioral changes. We addressed this by modeling evoked responses

using Dynamic Causal Modeling (DCM) to determine which connections differentiated stopping outcomes and scaled with SSRT across TFUS conditions. We considered a restricted network of areas that have consistently been found to be activated during inhibition. These areas include a fronto-parietal and cingulo-opercular network, centered around rIFG and pre-SMA, right temporal (rTemporal), right inferior occipital gyrus (rIOG), and right parietal (rParietal) areas (Levy & Wagner, 2011). To derive DCM locations for these sources, a source analysis on the mean difference between SS and US ERPs was performed in the 0-450 ms window. Source maps (**Fig. 5A**) revealed areas typically associated with successful inhibition. Maximal amplitudes of these source locations were used in the subsequent DCMs (see Methods).

We used a series of Bayesian model selections with family-wise random effects to determine the optimal structure by fitting different models to sensor responses during No-TFUS successful and unsuccessful inhibition trials from all subjects. The winning family for frontal hierarchies (**Fig. 5B**, top) included recurrent connections between rIFG and pSMA, with rIFG having top-down (backward) connectivity to pre-SMA (exceedance probability: 0.97). The family analysis examining the lower hierarchy (**Fig. 5B**, bottom) revealed rIOG was, as expected, connected to rTemp and rPC, but these two areas were not laterally connected (exceedance probability: 0.89). Finally, the comparisons examining lower-to-higher areas connections recapitulate known ventral and dorsal pathways (exceedance probability: 0.92). rIFG had top-down and bottom-up connectivity with rTemp, and pSMA had top-down projections to rPC and forward connections to pSMA. Finally, we found the best model to have inputs to both rIOG and rIFG (exceedance probability: 0.88).

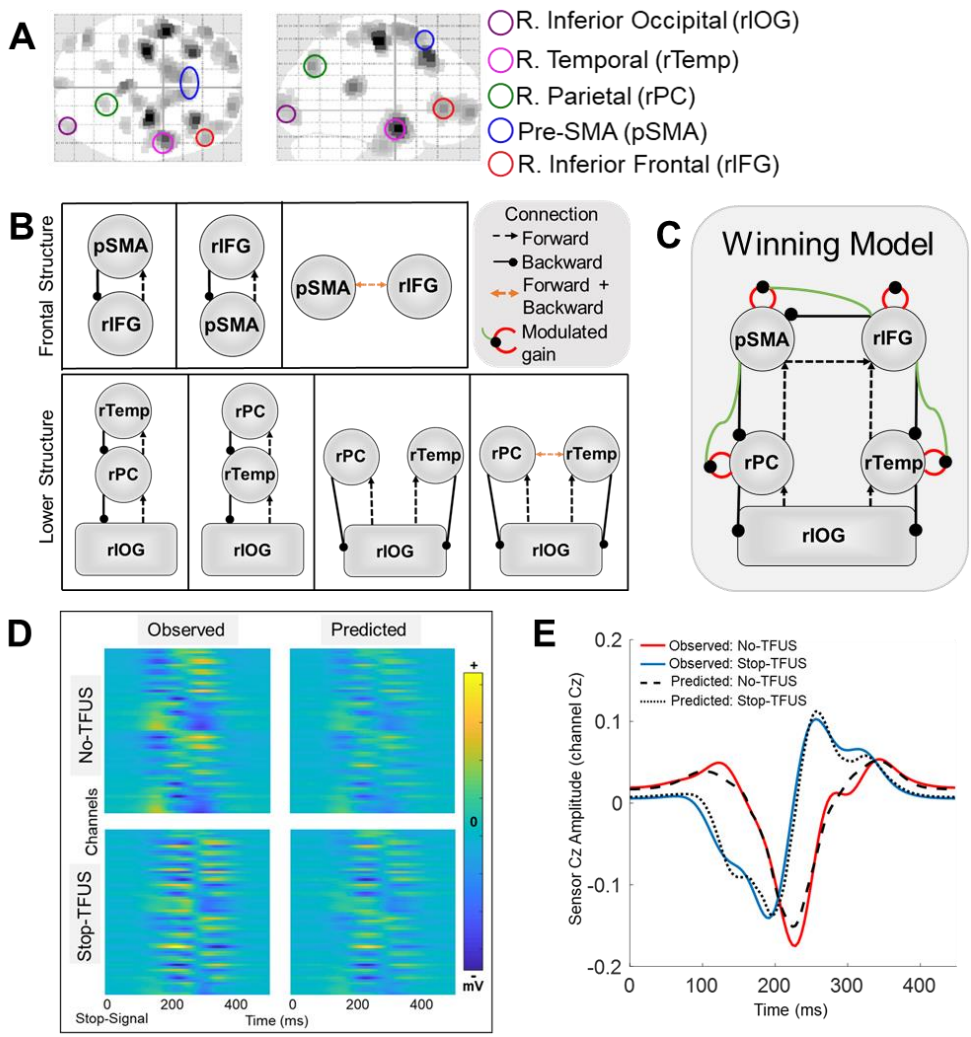

Figure 5 *Dynamic Causal modeling: Sources, structure, and fit.* **A.** Source map of grand mean ERP differences of SS minus US trials from 0 to 450 ms. Colored circled nodes denote center of node coordinates used for the 5 regions in the DCM. **B.** Configurational structures used to build base DC models and their connection types. **C.** Winning model showing the final configuration fit to individual subjects' data. **D.** Observed and predicted ERPs for all EEG channels for the average of No-TFUS and Stop-TFUS trials. **E.** Mean predicted (black dashed and dotted lines) and observed (red and blue lines) ERP from channel Cz plotted for successful Stop trials across No- and Stop-TFUS conditions, respectively. This plot shows that the modeled ERPs captured the TFUS-induced differences in N200 and P300 onsets and amplitudes.

Cortical control of stopping involves top-down rIFG gain control

A final set of model comparisons examined permutations of the above model with modulation of postsynaptic (recurrent) gain. We considered models wherein gain

changes occurred in either superficial pyramidal or inhibitory interneuron populations, and whether the post-synaptic gain effects were activity-independent or -dependent, and modulated by top-down activity. Model selection indicated strong evidence for a model with gain changes in inhibitory interneuron layers (probability: 0.96), all these effects being activity-dependent (probability: 0.93). Therefore, evoked activity during stopping was best explained by a network including gain changes that were dependent on top-down rIFG activity. The winning DCM used for further analysis is shown in **Figure 5C**. The core result from these model tests is that, although areas such as pSMA, rPC and rTemp are involved in generating inhibition-related ERPs, the network involved top-down, activity-dependent gain modulation from rIFG.

The optimized DCM structure (**Fig. 5C**) was fit to individual's evoked responses as separate models for the TFUS conditions. Fitted models accurately captured spatiotemporal properties of the ERP data across both sets of model fits (**Fig. 5D**) with an average fit of all DCM models of R^2 = 92% (±9%). **Figure 5E** shows the model faithfully captured characteristics of the N200 and P300 ERPs. The models were statistically analyzed in a parametric empirical Bayesian (PEB) model to determine which connections were modulated between SS and US trials and TFUS. As our hypotheses considered top-down coupling from rIFG and the effects of neurostimulation, for brevity we only consider these connections.

rIFG connections directly modulate with stopping outcomes

The main hypothesis was that rIFG regulates stopping via top-down gain modulation of inhibitory populations in pSMA. We predicted this modulation should be larger during successful inhibition. Model averaging over parameters corroborated this

hypothesis. Inhibitory interneuron gain modulation within rIFG and the rIFG to pSMA connectons increased during successful inhibitory trials. The direction of these effects for connections to fronto-parietal attention areas were reversed. During US trials, the rIFG to rTemp and pSMA to rPC gain was larger (**Fig. 6A**).

Because stopping propensity increased during TFUS, this motivated testing interactions of SS-US and TFUS on connectivity. The interaction of these parameters with TFUS were found in all of these connections. Intrinsic changes in rIFG gain, rIFG to pSMA, and pSMA to rPC gain modulation all exhibited interactions wherein the difference between US and SS trials was larger for Stop-TFUS trials (**Fig. 6B**). In contrast, the rIFG top-down modulation to rTemp was larger in the No-TFUS conditions. These effects point to an increased top-down modulation of rIFG connections and cascading onto rPC. In addition, the decreasing effect from rIFG to rTemp indicates stopping propensity was associated with a reduction of top-down coupling in the ventral pathway.

As the top-down effects from rIFG to pSMA resulted in disinhibition of inhibitory interneurons, this effectively increases top-down inhibition over pSMA through rIFG. A similar interpretation holds for the modulation of pSMA to rPC. To elaborate, increases (decreases) in self-recurrent gain of inhibitory interneurons have the effect of reducing (increasing) overall inhibition in the target area. Although several parameters correlated with change in behavioral inhibition, we further assessed the predictive validity of these connections as mediating stopping outcomes. This was tested by classifying the two stimulation conditions using a logistic regression, where the gain connections indexing SS-US trial differences were separately used to predict the TFUS condition class with a

10 k-fold cross-validation. Only the rIFG to pSMA (66% classification accuracy, $p < 0.05$) and the pSMA to rPC connection (77% classification accuracy, $p < 0.01$) were accurate predictors of TFUS conditional classes. Given the multiple top-down effects going from rIFG to pSMA and rPC, we reasoned the pSMA to rPC change was partially dependent on effects from rIFG to pSMA. We tested this by partialing effects of rIFG-to-pSMA connections on the latter with a linear regression, then re-running the classification using residuals. The pSMA to rPC classification accuracy was substantially reduced, but still significant (69%, $p < 0.01$).

rIFG connectivity modulates processing of stopping speed (SSRT)

The core behavioral finding was TFUS improved stopping by shortening SSRT. Accordingly, we predicted that if rIFG directly controlled inhibitory processes, its outgoing connectivity should reflect changes in SSRT across TFUS conditions. Connections were examined by comparing rIFG connectivity between SS trials with the SSRT difference as a covariate. Using No-TFUS trials as a baseline, we found the intrinsic rIFG gain, the rIFG-to-pSMA and pSMA-to-rPC inhibitory interneuron effects scaled with the difference in SSRT (**Fig. 6C**). Direction of these effects specifically reflected a decreasing gain from No-TFUS to Stop-TFUS, or a larger top-down inhibition scaling with shorter SSRTs. The core issue was reversing the problem and addressing whether any of these connection changes predicted the change in SSRT.

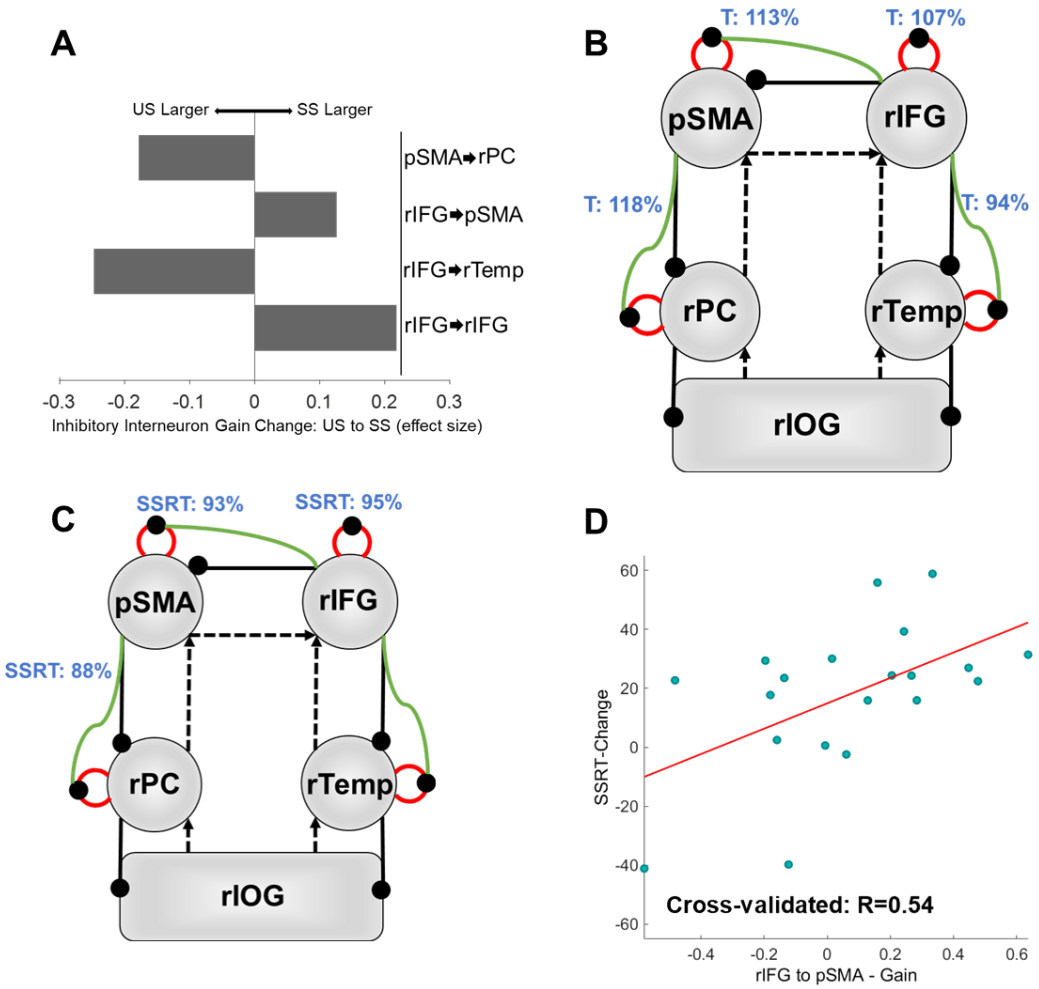

Figure 6 *Parametric empirical Bayesian analysis of Dynamic Causal models to distinguish overall success of stopping versus modulation with SSRT.* **A-B.** Results of PEB models for mean gain changes between SS and US trials in rIFG and their interactions with TFUS. **C**. PEB result showing parametric scaling of difference in SSRT between TFUS conditions with gain change between TFUS conditions for SS trials. **D**. Leave-one out cross-validated linear regression using rIFG to pre-SMA gain between (across TFUS conditions) SS trials as a predictor for the SSRT change.

We assessed the predictive strength for this SSRT effect using a leave-one out cross-validated robust linear regression. Supporting the hypothesis that rIFG-to-pSMA top-down gain modulation drives inhibition, we found it was the only significant predictor of this effective change in SSRT (R = 0.54, p = 0.013; **Fig. 6D**).

Beyond the connectivity modulation across TFUS conditions, our scalp analysis isolated P300 onset timing as a key marker of inhibitory outcomes and SSRT. A key question is: Where do the P300 effects emerge from, in terms of the local rIFG gain and its top-down inhibitory modulation over pre-SMA? The connection between scalp and source activity are visible in estimated deep pyramidal source activity for both areas (**Fig. 7**). We focus on deep layer activity because its strong correspondence with scalp ERPs. Timing differences in rIFG activity peaks reflected differences in stopping outcomes and SSRT. These behavioral effects were linked to a larger amplitude and earlier onset in rIFG (**Fig. 7**, top), respectively. As **Figure 6** shows, the success and its effective increase during TFUS conditions was associated with larger rIFG interneuron self-gain or increased disinhibition. The result is a larger deep pyramidal activity and top-down inhibitory modulation over pre-SMA. **Figure 7** (bottom) also shows the N200/P300 ERP complex was localized to pre-SMA. Comparing activity across areas indicated timing effects corresponding to SSRT were predominant in rIFG compared to pre-SMA, whereas pre-SMA exhibited a strong amplitude interaction across TFUS conditions. Together, these observations indicate rIFG activity reflected both inhibitory behavioral outcomes and neural response timing. The rIFG activity also points to P300 timing observed at the scalp as resulting from direct rIFG influence, rather than pre-SMA. Together, these results provide strong empirical support for top-down rIFG coupling driving response suppression through a direct inhibitory mechanism that directly links to timing of scalp P300 responses.

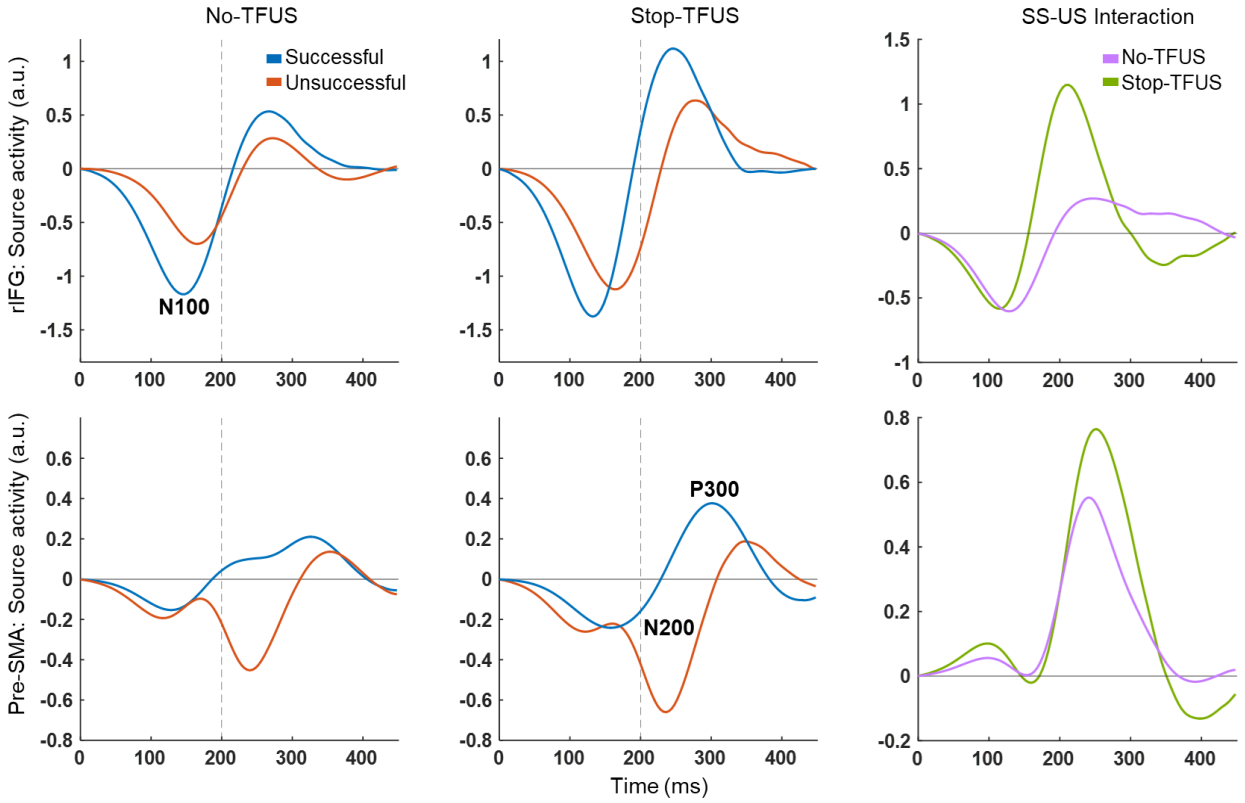

Figure 7 *rIFG source activity reflects inhibitory success and timing.* Top and bottom row plots show the estimated deep pyramidal source activity from rIFG and pSMA, respectively. The left and middle column plots show the comparison between successful and unsuccessful trials in the No-TFUS and Stop-TFUS conditions, respectively. The right column plots show the interaction between successful and unsuccessful trials (SS and US, respectively) in the No-TFUS and Stop-TFUS conditions.

Discussion

We provide causal evidence that rIFG directly drives response inhibition in the cortical network including pre-SMA through an inhibitory mechanism linked to ERPs. We demonstrated this relation by applying online transcranial focused ultrasound (TFUS) to human pars opercularis portion of rIFG during a stop-signal task. TFUS improved inhibitory performance with a faster stopping speed (SSRT) without impacting Go responses (**Fig. 3**).

We first sought to determine if an event-related potential (ERP) represents inhibitory components and could be isolated using TFUS. Inspired by correlative work (Wessel and Aron, 2015), EEG analysis revealed the P300 ERP onset tracked the SSRT and inhibitory success across TFUS conditions, supporting a causal connection to behavioral inhibition (**Fig. 4**). Our second goal was determining if the rIFG and pre-SMA network interactions exhibit the top-down inhibitory gain effects predicted by neural network models, while offering a causal explanation for P300 timing effects. Our approach of using Dynamic Causal Modeling (DCM) to test specific mechanisms driving evoked responses significantly extends previous findings. The modeling pointed to response inhibition being associated with a top-down rIFG modulation of inhibitory interneuron gain within pre-SMA (**Figs. 5-7**). To our knowledge, these findings provide the first demonstration of a causal link between rIFG and behavioral inhibition outcomes and potency, while simultaneously isolating the core neural markers and their basis in a mechanistically-specific neural inhibitory interaction in the rIFG and pre-SMA stopping network.

Our study builds on a robust neuroscience literature that has considered response inhibition from nearly all aspects. By employing online TFUS in parallel with EEG, we isolated P300 onset latencies as the sole predictor of behavioral outcomes – response inhibition performance and SSRT – during No-TFUS and Stop-TFUS trials. This result are consistent with recent work suggesting P300 latencies predict outcomes and SSRTs (Huster, Enriquez-Geppert, et al., 2013a; Wessel & Aron, 2015), with latency modulation occurring before but close to SSRT. This close temporal proximity of neural modulation and SSRT is predicted by Stop-Signal task studies of single units in

non-human primates (Hanes et al., 1998), as well as neural network (Lo et al., 2009) and accumulator models (Boucher et al., 2007; Logan et al., 2015). However, our work is the first to directly stimulate rIFG online and show a concurrent change in P300 onset and behavior. Consistent with other studies (Bekker et al., 2005; Kok et al., 2004), we also found the peak amplitudes of a posterior P100 and fronto-central N200 and P300 differentiated inhibitory outcomes. These effects were limited to No-TFUS trials, suggesting they reflect non-inhibitory processes, e.g., sensory detection (N100; Kenemans, 2015; Lijffijt et al., 2009), surprise or conflict (N200; Alexander & Brown, 2011; Enriquez-Geppert et al., 2010), or outcome-monitoring and attentionally-reoriented processing that could occur after the SSRT (P300; Corbetta et al., 2008; Polich, 2007).

It is worth noting the N200/P300 complex is regularly source localized to pre-SMA (or ACC; Enriquez-Geppert et al., 2010; Huster et al., 2013a), which might seem at odds with an inhibitory role of rIFG. However, we argue these results indicate rIFG interactions with pre-SMA are responsible for modulation of P300 timing. This proposition is consistent with the results of our modeling of ERPs. DCM optimization indicated rIFG governs inhibitory control through a top-down inhibitory coupling to pre-SMA. Model comparison pointed to rIFG connections explicitly related to stopping through a top-down, gain modulation over inhibitory interneurons in pre-SMA. This gain modulation was dependent on descending rIFG activity, i.e., voltage. Additionally, rIFG gain modulation was the only connection predictive of inhibitory success and SSRT across TFUS conditions. The key implication of these results is that stopping potency was causally related to rIFG activity levels directly increasing local inhibition in pre-SMA.

These conclusions diverge from previous fMRI work (Duann et al., 2009; Rae et al., 2015) that found rIFG to pre-SMA coupling predicts inhibitory success and SSRT, but also reported similarities across inhibitory and non-inhibitory tasks (Erika-Florence et al., 2014). Their interpretation was rIFG connectivity was a non-inhibitory process that signaled context-changes to pre-SMA. However, these studies only compared successful stopping against a baseline, without a pure comparison of stopping that we induced with TFUS.

Although we did not manipulate attention, our modeling also informs debates regarding rIFG connectivity as driving inhibitory versus attentional control (Aron et al., 2016; Hampshire & Sharp, 2015). We found rIFG to temporal and fronto-parietal pre-SMA to parietal connections interacted with inhibitory outcomes and TFUS. These ventral and fronto-parietal pathways, respectively, are typically associated with attentional reorienting (Corbetta et al., 2008; Vossel et al., 2014). Modulation of these pathways aligns with previous DCM studies explicitly manipulating top-down attention and stimulus expectancy (Auksztulewicz & Friston, 2015; Fardo et al., 2017). However, because we found that neither connection predicted SSRT, we expect these putatively attentional pathway effects are secondary to inhibitory effects exerted by rIFG on pre-SMA.

Both inhibitory and attentional frameworks predict rIFG exerts top-down gain modulation, which we considered during model building. However, they differ in which neural population gain should be modulated by rIFG. Building upon neural models of response inhibition (Lo et al., 2009; Logan et al., 2015) and circuit mechanisms (Roux & Buzsáki, 2015), there is agreement that direct inhibition is biologically plausible through

tuning of local inhibitory interneuron gain through interareal connections. In contrast, models underlying attention predicts top-down modulation or gain control over bottom-up excitation (Desimone & Duncan, 1995; Feldman & Friston, 2010; Spratling, 2008). DCM embeds excitatory gain through superficial pyramidal cells. Our formal model comparison was consistent with a direct inhibitory control model. The winning model involved rIFG modulating interneuron gain in pre-SMA (**Fig 5C**). This finding has a direct implication for explaining how rIFG could drive inhibition and how P300 onset timing in pre-SMA could reflect the behavioral timing of inhibitory responses.

The interpretation of these results rests on the effect of neural gain operating as a synaptic time-constant. Gain modulation can directly influence ERP timing of peaks and decay rates. This suggest the P300 onset tracking of SSRT was directed by rIFG activity levels that modulate inhibitory interneuron gain in pre-SMA. In turn, pre-SMA gain alters the expression of P300 timing. Two caveats are worth noting here. First, our model inferences are based on non-invasive measurements and require verification from invasive electrophysiology. Second, given rIFG's substantial morphological diversity and connectivity to other regions (Briggs et al., 2019) that are responsive to attentional and perceptual processing factors (Erika-Florence et al., 2014; Levy & Wagner, 2011), we expect our results indicate an explicit inhibitory function operates alongside other rIFG functions.

Most response inhibition analyses of non-invasive measures (EEG or MEG) have focused on sensor level analysis, some considering source activity (Enriquez-Geppert et al., 2010), or invasive electrophysiology with limited cortical coverage (Swann et al., 2012; Wessel et al., 2013). In contrast, a core focus of inhibition studies has been

identifying exact locations of activated regions and thus employed fMRI. However, this approach filters fast neural responses, with connectivity methods being agnostic to mechanistic instantiations of top-down and bottom-up interactions. We believe our utilization of ERPs, online TFUS, and DCM for evoked responses is most appropriate for differentiating bottom-up, top-down and gain effects driving evoked responses. This stems from the fact that theories of inhibition or attention predict different gain mechanisms, and these are instantiated in the microcircuit models within DCM (Bastos et al., 2012). While a clear limitation is indeterminacy with source localization (Grech et al., 2008), high temporal resolution is required to differentiate signals preceding stopping-related events, e.g., SSRT. These methodological concerns are tempered by pairing model-driven hypotheses with TFUS, because connectivity effects hold within the model across conditions despite source ambiguity. Finally, utilizing individual and accurate MRI-based head models increases accuracy of electromagnetic source models (Baillet et al., 2001). We also circumvented issues of relying on source localization to identify network nodes by a priori selecting regions identified from previous neuroimaging work (Levy & Wagner, 2011).

In conclusion, competing theories have argued whether response inhibition is a defining process of a cortical network centered on rIFG. Response inhibition likely involves several processes, ranging from sensory cue detection, attention, performance monitoring, and presumably explicit motor inhibition (Munakata, Herd, Chatham, Depue, Banich, & O'Reilly, 2011; Wessel & Aron, 2017; Wiecki & Frank, 2013). Our behavioral, ERP, and connectivity results favor the framework wherein rIFG is directly involved in explicit motor inhibition coinciding with attentional or sensory processing. The present

application of high-spatial resolution TFUS and ERP modeling provides a neural and methodological framework for testing other aspects of inhibitory and decision-making function. A key question is whether these gain mechanisms are the basis for global versus selective response inhibition. The efficacy of TFUS reported here also indicates a possible neural intervention to pair with treatment for behavioral disorders stemming from inhibitory response dysfunction, e.g., impulsivity or ADHD (Bari & Robbins, 2013).

References

Alexander, W. H., & Brown, J. W. (n.d.). *Medial prefrontal cortex as an action-outcome predictor*. https://doi.org/10.1038/nn.2921

Aron, A. R. (2006). Cortical and Subcortical Contributions to Stop Signal Response Inhibition: Role of the Subthalamic Nucleus. *Journal of Neuroscience*. https://doi.org/10.1523/JNEUROSCI.4682-05.2006

Aron, Adam R. (2011). *From Reactive to Proactive and Selective Control: Developing a Richer Model for Stopping Inappropriate Responses*. https://doi.org/10.1016/j.biopsych.2010.07.024

Aron, Adam R, Fletcher, P. C., Bullmore, E. T., Sahakian, B. J., & Robbins, T. W. (2003). *Stop-signal inhibition disrupted by damage to right inferior frontal gyrus in humans*. 2002–2003. https://doi.org/10.1038/nn1003

Aron, Adam R, Herz, D. M., Brown, X. P., Forstmann, B. U., & Zaghloul, K. (2016). *Frontosubthalamic Circuits for Control of Action and Cognition*. *36*(45), 11489–11495. https://doi.org/10.1523/JNEUROSCI.2348-16.2016

Aron, Adam R, Robbins, T. W., & Poldrack, R. A. (2014). Inhibition and the right inferior frontal cortex : one decade on. *Trends in Cognitive Sciences*, *18*(4), 177–185. https://doi.org/10.1016/j.tics.2013.12.003

Aubry, J.-F., Tanter, M., Pernot, M., Thomas, J.-L., & Fink, M. (2003). Experimental demonstration of noninvasive transskull adaptive focusing based on prior computed tomography scans. *The Journal of the Acoustical Society of America*. https://doi.org/10.1121/1.1529663

Auksztulewicz, R., & Friston, K. (2015). Attentional enhancement of auditory mismatch responses: A DCM/MEG study. *Cerebral Cortex*. https://doi.org/10.1093/cercor/bhu323

Baillet, S., Rira, J. J., Main, G., Magin, J. F., Aubert, J., & Ganero, L. (2001). Evaluation of inverse methods and head models for EEG source localization using a human skull phantom. *Physics in Medicine and Biology*. https://doi.org/10.1088/0031-9155/46/1/306

Bari, A., & Robbins, T. W. (2013). Inhibition and impulsivity: Behavioral and neural basis of response control. In *Progress in Neurobiology*. https://doi.org/10.1016/j.pneurobio.2013.06.005

Bastos, A. M., Usrey, W. M., Adams, R. A., Mangun, G. R., Fries, P., & Friston, K. J. (2012). Perspective Canonical Microcircuits for Predictive Coding. *Neuron*, *76*(4), 695–711. https://doi.org/10.1016/j.neuron.2012.10.038

Bekker, E. M., Kenemans, J. L., Hoeksma, M. R., Talsma, D., & Verbaten, M. N. (2005). The pure electrophysiology of stopping. *International Journal of Psychophysiology*. https://doi.org/10.1016/j.ijpsycho.2004.07.005

Belardinelli, P., Ortiz, E., Barnes, G., Noppeney, U., & Preissl, H. (2012). Source Reconstruction Accuracy of MEG and EEG Bayesian Inversion Approaches. *PLoS ONE*, *7*(12). https://doi.org/10.1371/journal.pone.0051985

Boehler, C. (2010). Pinning down response inhibition in the brain-conjunction analyses of the Stop-signal task4). *Neuroimage*, *52*(1), 1621–1632. https://doi.org/10.1016/j.neuroimage.2010.04.276

Boucher, L., Palmeri, T. J., Logan, G. D., & Schall, J. D. (2007). Inhibitory control in mind and brain: An interactive race model of countermanding saccades. *Psychological Review*. https://doi.org/10.1037/0033-295X.114.2.376

Briggs, R. G., Chakraborty, A. R., Anderson, C. D., Abraham, C. J., Palejwala, A. H., Conner, A. K., Pelargos, P. E., O'Donoghue, D. L., Glenn, C. A., & Sughrue, M. E. (2019). Anatomy and white matter connections of the inferior frontal gyrus. *Clinical Anatomy*. https://doi.org/10.1002/ca.23349

Brown, H., Friston, K., & Bestmann, S. (2011). *Active inference , attention , and motor preparation*. *2*(September), 1–10. https://doi.org/10.3389/fpsyg.2011.00218

Brown, H. R., & Friston, K. J. (2012). Dynamic causal modelling of precision and synaptic gain in visual perception - an EEG study. *NeuroImage*. https://doi.org/10.1016/j.neuroimage.2012.06.044

Chikazoe, J., Jimura, K., Hirose, S., Yamashita, K. I., Miyashita, Y., & Konishi, S. (2009). Preparation to inhibit a response complements response inhibition during performance of a stop-signal task. *Journal of Neuroscience*. https://doi.org/10.1523/JNEUROSCI.3645-09.2009

Corbetta, M., Patel, G., & Shulman, G. L. (2008). The Reorienting System of the Human Brain: From Environment to Theory of Mind. In *Neuron*. https://doi.org/10.1016/j.neuron.2008.04.017

Deco, G., & Rolls, E. T. (2005). Neurodynamics of biased competition and cooperation for attention: A model with spiking neurons. *Journal of Neurophysiology*. https://doi.org/10.1152/jn.01095.2004

Delorme, A., & Makeig, S. (2004). EEGLAB: An open source toolbox for analysis of single-trial EEG dynamics including independent component analysis. *Journal of Neuroscience Methods*, *134*(1), 9–21. https://doi.org/10.1016/j.jneumeth.2003.10.009

Desimone, R., & Duncan, J. (1995). Neural Mechanisms of Selective Visual Attention. *Annual Review of Neuroscience*. https://doi.org/10.1146/annurev.ne.18.030195.001205

Duann, J.-R., Ide, J. S., Luo, X., & Li, C. R. (2009). Functional connectivity delineates distinct roles of the inferior frontal cortex and presupplementary motor area in stop signal inhibition. *The Journal of Neuroscience : The Official Journal of the Society for Neuroscience*, *29*(32), 10171–10179. https://doi.org/10.1523/JNEUROSCI.1300-09.2009

Enriquez-Geppert, S., Konrad, C., Pantev, C., & Huster, R. J. (2010). Conflict and inhibition differentially affect the N200/P300 complex in a combined go/nogo and stop-signal task. *NeuroImage*, *51*(2), 877–887. https://doi.org/10.1016/J.NEUROIMAGE.2010.02.043

Erika-Florence, M., Leech, R., & Hampshire, A. (2014). A functional network perspective on response inhibition and attentional control. *Nature Communications*. https://doi.org/10.1038/ncomms5073

Fardo, F., Auksztulewicz, R., Allen, M., Dietz, M. J., Roepstorff, A., & Friston, K. J. (2017). Expectation violation and attention to pain jointly modulate neural gain in somatosensory cortex. *NeuroImage*. https://doi.org/10.1016/j.neuroimage.2017.03.041

Feldman, H., & Friston, K. J. (2010). Attention, Uncertainty, and Free-Energy. *Frontiers in Human Neuroscience*, *4*(December), 1–23. https://doi.org/10.3389/fnhum.2010.00215

Friston, K. J., Litvak, V., Oswal, A., Razi, A., Stephan, K. E., Van Wijk, B. C. M., Ziegler, G., & Zeidman, P. (2016). Bayesian model reduction and empirical Bayes for group (DCM) studies. *NeuroImage*. https://doi.org/10.1016/j.neuroimage.2015.11.015

Grech, R., Cassar, T., Muscat, J., Camilleri, K. P., Fabri, S. G., Zervakis, M., Xanthopoulos, P., Sakkalis, V., & Vanrumste, B. (2008). Review on solving the inverse problem in EEG source analysis. In *Journal of NeuroEngineering and Rehabilitation*. https://doi.org/10.1186/1743-0003-5-25

Greenhouse, I., & Wessel, J. R. (2013). *EEG signatures associated with stopping are sensitive to preparation*. https://doi.org/10.1111/psyp.12070

Hampshire, A., Chamberlain, S. R., Monti, M. M., Duncan, J., & Owen, A. M. (2010). The role of the right inferior frontal gyrus: inhibition and attentional control. *Neuroimage*, *50*(3–3), 1313. https://doi.org/10.1016/J.NEUROIMAGE.2009.12.109

Hampshire, A., & Sharp, D. J. (2015). Contrasting network and modular perspectives on inhibitory control. In *Trends in Cognitive Sciences*. https://doi.org/10.1016/j.tics.2015.06.006

Hanes, D. P., Patterson, W. F., & Schall, J. D. (1998). Role of frontal eye fields in countermanding saccades: Visual, movement, and fixation activity. *Journal of Neurophysiology*. https://doi.org/10.1152/jn.1998.79.2.817

Huster, R. J., Enriquez-geppert, S., Lavallee, C. F., Falkenstein, M., & Herrmann, C. S. (2013). Electroencephalography of response inhibition tasks : Functional networks and cognitive contributions. *International Journal of Psychophysiology*, *87*(3), 217–233. https://doi.org/10.1016/j.ijpsycho.2012.08.001

Huster, R. J., Enriquez-Geppert, S., Lavallee, C. F., Falkenstein, M., & Herrmann, C. S. (2013a). Electroencephalography of response inhibition tasks: Functional networks and cognitive contributions. In *International Journal of Psychophysiology*. https://doi.org/10.1016/j.ijpsycho.2012.08.001

Huster, R. J., Enriquez-Geppert, S., Lavallee, C. F., Falkenstein, M., & Herrmann, C. S. (2013b). *Electroencephalography of response inhibition tasks: Functional networks and cognitive contributions*. https://doi.org/10.1016/j.ijpsycho.2012.08.001

Kenemans, J. L. (2015). Specific proactive and generic reactive inhibition. In *Neuroscience and Biobehavioral Reviews*. https://doi.org/10.1016/j.neubiorev.2015.06.011

Kibleur, A., Gras-Combe, G., Benis, D., Bastin, J., Bougerol, T., Chabardès, S., Polosan, M., & David, O. (2016). Modulation of motor inhibition by subthalamic stimulation in obsessive-compulsive disorder. *Translational Psychiatry*, *6*, 922. https://doi.org/10.1038/tp.2016.192

Kok, A., Ramautar, J. R., De Ruiter, M. B., Band, G. P. H., & Ridderinkhof, K. R. (2004). ERP components associated with successful and unsuccessful stopping in a stop-signal task. *Psychophysiology*. https://doi.org/10.1046/j.1469-8986.2003.00127.x

Legon, W., Bansal, P., Tyshynsky, R., Ai, L., & Mueller, J. K. (2018). Transcranial focused ultrasound neuromodulation of the human primary motor cortex. *Scientific Reports*. https://doi.org/10.1038/s41598-018-28320-1

Legon, W., Sato, T. F., Opitz, A., Mueller, J., Barbour, A., Williams, A., & Tyler, W. J. (2014). Transcranial focused ultrasound modulates the activity of primary somatosensory cortex in humans. *Nature Neuroscience*. https://doi.org/10.1038/nn.3620

Levy, B. J., & Wagner, A. D. (2011). Cognitive control and right ventrolateral prefrontal cortex: reflexive reorienting, motor inhibition, and action updating. *Ann. N.Y. Acad. Sci*. https://doi.org/10.1111/j.1749-6632.2011.05958.x

Lijffijt, M., Lane, S. D., Meier, S. L., Boutros, N. N., Burroughs, S., Steinberg, J. L., Gerard Moeller, F., & Swann, A. C. (2009). P50, N100, and P200 sensory gating: Relationships with behavioral inhibition, attention, and working memory. *Psychophysiology*. https://doi.org/10.1111/j.1469-8986.2009.00845.x

Lo, C. C., Boucher, L., Paré, M., Schall, J. D., & Wang, X. J. (2009). Proactive inhibitory control and attractor dynamics in countermanding action: A spiking neural circuit model. *Journal of Neuroscience*. https://doi.org/10.1523/JNEUROSCI.6164-08.2009

Logan, G. D., & Cowan, W. B. (1984). On the ability to inhibit thought and action: A theory of an act of control. *Psychological Review*. https://doi.org/10.1037/0033-295X.91.3.295

Logan, G. D., Yamaguchi, M., Schall, J. D., & Palmeri, T. J. (2015). Inhibitory control in mind and brain 2.0: Blocked-input models of saccadic countermanding. *Psychological Review*. https://doi.org/10.1037/a0038893

Lovett-Barron, M., Turi, G. F., Kaifosh, P., Lee, P. H., Bolze, F., Sun, X. H., Nicoud, J. F., Zemelman, B. V., Sternson, S. M., & Losonczy, A. (2012). Regulation of neuronal input transformations by tunable dendritic inhibition. *Nature Neuroscience*. https://doi.org/10.1038/nn.3024

Mathôt, S., Schreij, D., & Theeuwes, J. (2012). OpenSesame: An open-source, graphical experiment builder for the social sciences. In *Behavior Research Methods*. https://doi.org/10.3758/s13428-011-0168-7

Mattia, M., Spadacenta, S., Pavone, L., Quarato, P., Esposito, V., Sparano, A., Sebastiano, F., Di Gennaro, G., Morace, R., Cantore, G., & Mirabella, G. (2012). Stop-event-related potentials from intracranial electrodes reveal a key role of premotor and motor cortices in stopping ongoing movements. *Frontiers in Neuroengineering*. https://doi.org/10.3389/fneng.2012.00012

Moran, R. (2015). Dynamic Causal Models for Human Electrophysiology: EEG, MEG, and LFPs. *Brain Mapping*, 625–628. https://doi.org/10.1016/B978-0-12-397025-1.00340-7

Moran, R. J., Campo, P., Symmonds, M., Stephan, K. E., Dolan, R. J., & Friston, K. J. (2013). Free energy, precision and learning: The role of cholinergic neuromodulation. *Journal of Neuroscience*. https://doi.org/10.1523/JNEUROSCI.4255-12.2013

Mostofsky, S. H., & Simmonds, D. J. (2008). Response inhibition and response selection: Two sides of the same coin. In *Journal of Cognitive Neuroscience*. https://doi.org/10.1162/jocn.2008.20500

Munakata, Y., Herd, S. A., Chatham, C. H., Depue, B. E., Banich, M. T., & O'reilly, R. C. (2011). A unified framework for inhibitory control Opinion. *Trends in Cognitive Sciences*, *15*(10), 453–459. https://doi.org/10.1016/j.tics.2011.07.011

Munakata, Y., Herd, S. A., Chatham, C. H., Depue, B. E., Banich, M. T., & O'Reilly, R. C. (2011). A unified framework for inhibitory control. In *Trends in Cognitive Sciences*. https://doi.org/10.1016/j.tics.2011.07.011

Polich, J. (2007). Updating P300: An integrative theory of P3a and P3b. In *Clinical Neurophysiology*. https://doi.org/10.1016/j.clinph.2007.04.019

Rae, C. L., Hughes, L. E., Anderson, M. C., & Rowe, J. B. (2015). The prefrontal cortex achieves inhibitory control by facilitating subcortical motor pathway connectivity. *Journal of Neuroscience*. https://doi.org/10.1523/JNEUROSCI.3093-13.2015

Roux, L., & Buzsáki, G. (2015). Tasks for inhibitory interneurons in intact brain circuits. In *Neuropharmacology*. https://doi.org/10.1016/j.neuropharm.2014.09.011

Rushworth, M. F. S., Walton, M. E., Kennerley, S. W., & Bannerman, D. M. (2004). Action sets and decisions in the medial frontal cortex. In *Trends in Cognitive Sciences*. https://doi.org/10.1016/j.tics.2004.07.009

Sharp, D. J., Bonnelle, V., De Boissezon, X., Beckmann, C. F., James, S. G., Patel, M. C., & Mehta, M. A. (2010). Distinct frontal systems for response inhibition, attentional capture, and error processing. *Proceedings of the National Academy of Sciences of the United States of America*. https://doi.org/10.1073/pnas.1000175107

Spratling, M. W. (2008). Reconciling predictive coding and biased competition models of cortical function. *Frontiers in Computational Neuroscience*. https://doi.org/10.3389/neuro.10.004.2008

Swann, N. C., Cai, W., Conner, C. R., Pieters, T. A., Claffey, M. P., George, J. S., Aron, A. R., & Tandon, N. (2011). *NeuroImage Roles for the pre-supplementary motor area and the right inferior frontal gyrus in stopping action : Electrophysiological responses and functional and structural connectivity*. https://doi.org/10.1016/j.neuroimage.2011.09.049

Swann, N. C., Cai, W., Conner, C. R., Pieters, T. A., Claffey, M. P., George, J. S., Aron, A. R., & Tandon, N. (2012). "Roles for the pre-supplementary motor area and the right inferior frontal gyrus in stopping action: electrophysiological responses and functional and structural connectivity." *NeuroImage*, *59*(3), 2860–2870. https://doi.org/10.1016/j.neuroimage.2011.09.049

Thiele, A., & Bellgrove, M. A. (2018). Neuromodulation of Attention. In *Neuron*. https://doi.org/10.1016/j.neuron.2018.01.008

Treeby, B. E., & Cox, B. T. (2010). k-Wave: MATLAB toolbox for the simulation and reconstruction of photoacoustic wave fields. *Journal of Biomedical Optics*. https://doi.org/10.1117/1.3360308

Vossel, S., Geng, J. J., & Fink, G. R. (2014). Dorsal and ventral attention systems: Distinct neural circuits but collaborative roles. *Neuroscientist*. https://doi.org/10.1177/1073858413494269

Wessel, J. R., & Aron, A. R. (2015). It's not too late: The onset of the frontocentral P3 indexes successful response inhibition in the stop-signal paradigm. *Psychophysiology*, *52*(4), 472–480. https://doi.org/10.1111/psyp.12374

Wessel, J. R., & Aron, A. R. (2017). On the Globality of Motor Suppression: Unexpected Events and Their Influence on Behavior and Cognition. In *Neuron*. https://doi.org/10.1016/j.neuron.2016.12.013

Wessel, J. R., Conner, C. R., Aron, A. R., & Tandon, N. (2013). Chronometric electrical stimulation of right inferior frontal cortex increases motor braking. *Journal of Neuroscience*. https://doi.org/10.1523/JNEUROSCI.3468-13.2013

Wiecki, T. V, & Frank, M. J. (2013). *A Computational Model of Inhibitory Control in Frontal Cortex and Basal Ganglia*. *120*(2), 329–355. https://doi.org/10.1037/a0031542